Newton

Article

Dynamically resolved evolution and quantitative mapping of conformal skyrmion lattice

Graphical abstract

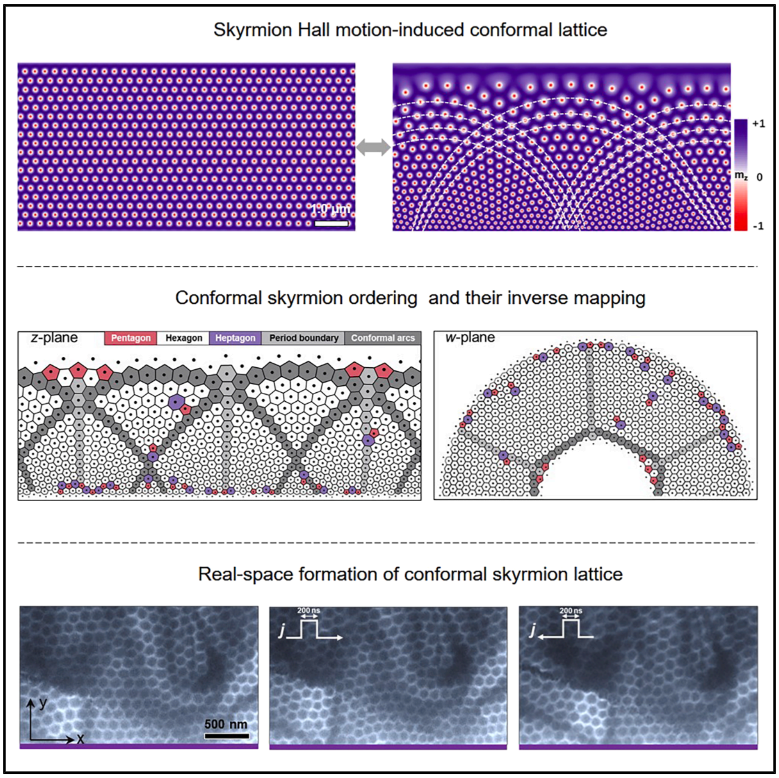

Highlights

- Skyrmion Hall motion drives the assembly of a conformal skyrmion lattice
- Machine vision tracks skyrmion defects, curvature, and Hall-angle redistribution
- Inverse conformal mapping restores the compressed skyrmion lattice to hexagonal order
- Lorentz TEM observes conformal skyrmion ordering in $Co_9Zn_9Mn_2$

Authors

Wenkun Zhao, Shangrun Lu,
Qingfa Luo, ..., Jinbo Yang, Yanglong Hou,
Licong Peng

Correspondence

zhaogp@uestc.edu.cn (G.Z.),
jbyang@pku.edu.cn (J.Y.),
hou@pku.edu.cn (Y.H.),
licong.peng@pku.edu.cn (L.P.)

In brief

Understanding how skyrmion crystals reorganize under driving is central to geometry-enabled spintronics. Zhao et al. show that skyrmion Hall-motion-driven lateral compression builds lattice curvature and triggers defect-mediated reorganization, producing a conformal skyrmion lattice with spatial gradients in skyrmion density and size while maintaining local angular order. Inverse conformal mapping quantitatively verifies conformality, and Lorentz transmission electron microscopy observes the conformal skyrmion ordering in $Co_9Zn_9Mn_2$. Such geometry-controlled lattices offer a tunable source of stochastic bits for true random-number generation.

Zhao et al., 2026, Newton *2*, 100443
July 6, 2026
https://doi.org/10.1016/j.newton.2026.100443

CellPress

Please cite this article in press as: Zhao et al., Dynamically resolved evolution and quantitative mapping of conformal skyrmion lattice, Newton (2026), https://doi.org/10.1016/j.newton.2026.100443

Newton

CellPress
OPEN ACCESS

Article

Dynamically resolved evolution and quantitative mapping of conformal skyrmion lattice

Wenkun Zhao,[1,2,7] Shangrun Lu,[1,7] Qingfa Luo,[1,2] Xichao Zhang,[3] Shaohua Fan,[4,5] Haoting Lu,[1] Guanghui Han,[1] Tianyu Xin,[4] Zhaochu Luo,[4] Guoping Zhao,[2,*] Jinbo Yang,[4,*] Yanglong Hou,[1,6,*] and Licong Peng[1,8,*]

[1]School of Materials Science and Engineering, Peking University, Beijing 100871, China
[2]College of Physics and Electronic Engineering, Sichuan Normal University, Chengdu 610068, China
[3]Department of Applied Physics, Waseda University, Okubo, Shinjuku, Tokyo 169-8555, Japan
[4]State Key Laboratory for Mesoscopic Physics, School of Physics, Peking University, Beijing 100871, China
[5]Key Laboratory of Magnetic Molecules and Magnetic Information Materials of Ministry of Education, School of Materials Science and Engineering, Shanxi Normal University, Taiyuan 030031, China
[6]School of Materials, Shenzhen Campus of Sun Yat-sen University, Shenzhen 518107, China
[7]These authors contributed equally
[8]Lead contact
*Correspondence: zhaogp@uestc.edu.cn (G.Z.), jbyang@pku.edu.cn (J.Y.), hou@pku.edu.cn (Y.H.), licong.peng@pku.edu.cn (L.P.)
https://doi.org/10.1016/j.newton.2026.100443

ACCESSIBLE OVERVIEW Magnetic skyrmions are nanoscale topologically protected spin textures that can be efficiently driven by electric currents, making them attractive information carriers for skyrmion-based memory and unconventional computing. Beyond single-particle behavior, skyrmions readily self-organize under confinement and external perturbations, producing collective states with rich geometry and dynamics. One particularly intriguing phenomenon is a conformal lattice: a structure with smoothly varying density and curvature while retaining local crystalline order, typically emerging through defect-mediated reorganization under spatial constraints. Conformal ordering has been studied in colloids and superconducting vortex matter, but its formation mechanism and real-space observation in magnetic skyrmion systems remain elusive. In this work, we track, in real time, how the skyrmion Hall effect drives lateral compression and reshapes a hexagonal skyrmion lattice into a conformal state. By integrating micromagnetic simulations with machine-vision trajectory analysis, we resolve the full reorganization process and quantify its key signatures: progressive curvature buildup, layer-dependent redistribution of Hall angles, and defect-mediated rearrangements that reshape global order while preserving local orientational coherence. To verify whether the resulting pattern is intrinsically conformal, we use inverse conformal mapping as a quantitative approach and demonstrate local angle preservation throughout the distorted lattice. We further realize conformal skyrmion ordering experimentally in $Co_9Zn_9Mn_2$ using Lorentz transmission electron microscopy, providing direct support for the simulated mechanism. Our combined time-resolved tracking, inverse conformal mapping, and experimental observations make conformal skyrmion ordering a verifiable and engineerable collective state, with promise for geometry-tunable stochasticity in true random-number generation.

SUMMARY

Conformal lattices, characterized by spatially varying yet locally ordered structures, have been studied in colloidal and superconducting systems. However, their quantitative validation and underlying formation mechanisms in magnetic skyrmion systems remain largely unexplored. In this work, we dynamically resolve the formation of conformal skyrmion lattices induced by lateral compression driven by the skyrmion Hall effect. Combining micromagnetic simulations with machine-vision trajectory tracking, we reveal the evolution of lattice curvature, layer-dependent skyrmion Hall-angle redistribution, and defect generation. The conformality of the emergent lattice is rigorously verified through inverse conformal mapping, quantitatively confirming local angular preservation, while force analysis reveals an exponentially decaying repulsive interaction that underpins lattice formation. We further show that conformal skyrmion lattices can be experimentally realized and reversibly controlled in $Co_9Zn_9Mn_2$ using nanosecond current pulses, in agreement with our

Please cite this article in press as: Zhao et al., Dynamically resolved evolution and quantitative mapping of conformal skyrmion lattice, Newton (2026), https://doi.org/10.1016/j.newton.2026.100443

simulations. These results provide a quantitative approach to understanding conformal skyrmion geometries and suggest their potential for stochastic bit generation.

INTRODUCTION

Two-dimensional many-body systems often self-organize to accommodate boundary constraints or external perturbations, giving rise to rich collective dynamics and emergent structural phenomena.[1–3] Topological defects such as dislocations and disclinations commonly arise in these two-dimensional assemblies, distorting local lattice geometry and disrupting global orientational order.[4–6] Crucially, these defects also mediate structural transitions, including disordering into fluid-like states[3,7,8] or reorganization into alternative ordered phases such as conformal lattices,[9,10] where local hexagonal symmetry is preserved while the global structure smoothly adapts to spatial inhomogeneity. Such defect-mediated structural transitions have attracted significant interest, particularly in magnetic-particle systems, due to their complex interactions and dissipative dynamics.[3,8,11–13]

Magnetic skyrmions are topologically protected quasiparticles with nanoscale dimensions and high current-driven mobility,[14–16] making them promising candidates for current-controlled information carriers in spintronic applications such as skyrmion-based memory[17] and unconventional computing functionalities (e.g., logic,[18,19] neuromorphic,[20,21] and stochastic signal generation[22,23]). Recent experiments have demonstrated increasingly precise current-driven manipulation of skyrmions, including the motion of individual skyrmions,[24,25] guided translation along nanostripes,[26,27] and notch-assisted nucleation and annihilation.[28,29] Beyond such single-skyrmion control, their topological stability and structural flexibility enable dynamic modulation in size and shape under external drive,[30–32] while mutual interparticle interactions govern their collective spatial arrangements.[33,34] Thermal gradients can drive ratchet-like motion in skyrmion ensembles and induce topological magnon Hall effects.[35,36] When subjected to current-induced spin-transfer torque, dense skyrmion lattices experience lateral movement due to the skyrmion Hall effect[11,37] (Figure 1A), leading to accumulation near boundaries.[38,39] Near edges, skyrmions may annihilate, elastically rebound, or shrink, depending on whether the skyrmion-edge interactions are attractive or repulsive.[40–42] The boundary effect, together with mutual interactions, can reorganize lattice geometry and promote the emergence of conformal lattice structures.[10,43] Conformal ordering has been explored in colloidal and vortex systems,[44,45] where geometric transformations and force-based models are used to quantify angular preservation and density adaptation.[46,47] However, in magnetic skyrmion systems, the structural evolution of conformal states and the underlying mechanisms remain largely unexplored.

In this work, we dynamically resolve the formation of conformal skyrmion lattices and quantitatively validate their geometry using inverse transformation mapping and force-analysis models. We reveal the time-resolved evolution of topological defects through machine-vision tracking, accompanied by curvature buildup and Hall-angle redistribution, which collectively drive the phase transition from a regular hexagonal lattice to a conformal ordered state through defect-mediated reorganization. Importantly, we experimentally realize conformal skyrmion lattice in $Co_9Zn_9Mn_2$, in agreement with our simulations.

RESULTS

Skyrmion Hall-motion-induced conformal ordering

We simulate a system initialized with a hexagonal skyrmion lattice (SKL) under a perpendicular magnetic field (B_z) of 300 mT (Figure 1B) (see methods). Periodic boundary conditions are applied along the x direction, while the y direction is confined by rigid boundaries. When a current density of $j_x = 4 \times 10^{10}$ A/m^2 is applied along the $+x$ direction, skyrmions move not only along the current but also drift toward the boundary, due to the spin-transfer torque-driven skyrmion Hall effect (Figure 1A). As a result, the initially uniform hexagonal lattice gradually evolves into a compressed configuration with a pronounced gradient in skyrmion size and density along the y axis (see Video S1), forming an arch-like spatial profile. This emergent structure, referred to as a conformal skyrmion lattice, is given in Figure 1C, where white dashed lines trace continuous arcs, highlighting the curvature across the entire lattice.

To quantitatively characterize this deformation, we extract the time-dependent curvature $\rho = 1/R$ of the arc lines (Figure 1D), where R denotes the local radius of curvature. The curvature is obtained by tracing skyrmion-core trajectories derived from magnetization maps and graph-based algorithms (see Figure S1 and methods). When applying the electric current, the lattice undergoes topological rearrangement, marked by skyrmion compression and increasing curvature. This evolution saturates around $t = 700$ ns, indicating the formation of a stable conformal SKL. Meanwhile, we analyzed the skyrmion size and density distributions along the y direction (Figure 1E). Initially, the lattice is uniform, with a characteristic skyrmion radius r of approximately 82 nm (dashed line). After compression, r exhibits a vertical gradient, ranging from 35 nm to 103 nm, with smaller, denser skyrmions accumulating at the bottom and larger, more diluted ones appearing toward the top. Despite this gradient, the local structure retains near-hexagonal geometry with angles close to 120°, consistent with a conformal transformation that preserves local angles while varying global scale.[9]

We further examine how the magnetic field strength affects conformal SKL stability by monitoring the topological charge Q, which reflects the overall integrity of skyrmions. The decay of Q results from skyrmion annihilation near the boundaries, where the combined effect of current-induced drift and skyrmion-edge interactions drives skyrmions outward and destabilizes the lattice. The field dependence of ΔQ (annihilation number of skyrmions) is shown in Figure 1F, while its time evolution is presented in Figure S3. At low fields, skyrmions near the upper boundary are elongated due to edge pinning, forming stripe-like distortions that disrupt the lattice order. At high fields, skyrmions shrink under stronger Zeeman energy, and overcompression further reduces their stability, leading to annihilation. In both cases, the significant loss of skyrmions prevents the

Please cite this article in press as: Zhao et al., Dynamically resolved evolution and quantitative mapping of conformal skyrmion lattice, Newton (2026), https://doi.org/10.1016/j.newton.2026.100443

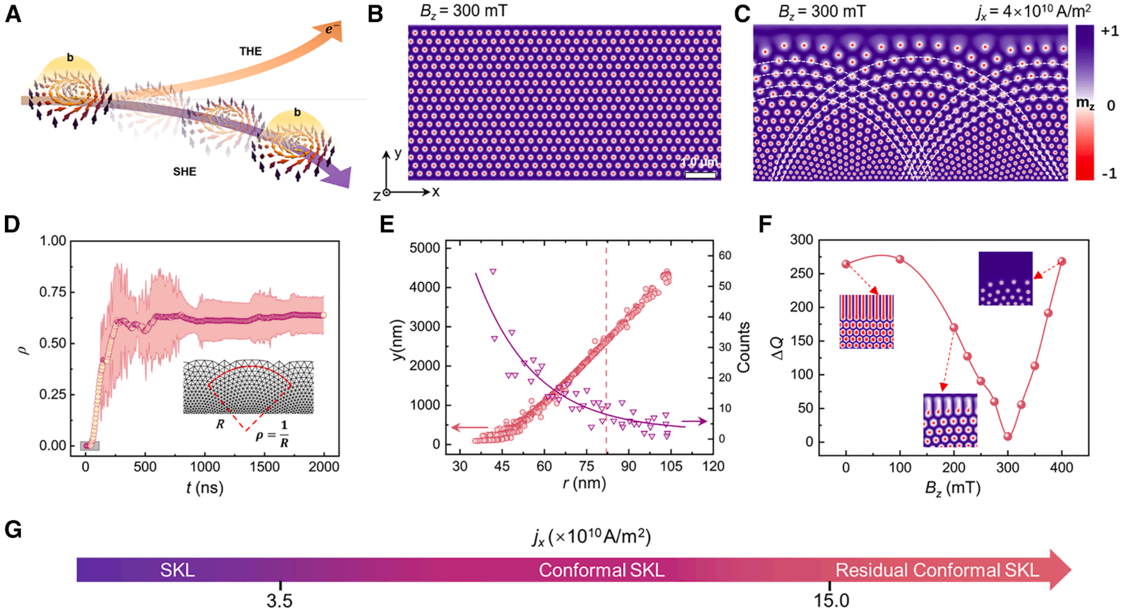

Figure 1. Skyrmion Hall-motion-induced conformal ordering

(A) Illustration of the electron-skyrmion interaction. The emergent magnetic field *b* deflects electrons (topological Hall effect [THE]), and the reactive force drives skyrmion transverse motion (skyrmion Hall effect [SHE]).

(B and C) Simulated configurations of (B) hexagonal skyrmion lattice (SKL) under 300 mT and (C) conformal SKL after applying an electric current of $j_x = 4 \times 10^{10}$ A/m^2 along the +*x* direction for 2,000 ns. White dashed arcs indicate conformal alignment. The color code represents the out-of-plane magnetization component m_z.

(D) Time evolution of the normalized average curvature $\rho = 1/R$ extracted from skyrmion trajectories (inset); the pink shaded area shows the standard deviation of the curvature.

(E) Skyrmion radius variation along the *y* axis showing a gradual compression gradient (left), with the dashed line indicating the initial radius. The corresponding distribution of skyrmion counts as a function of radius is shown on the right.

(F) Topological charge variation ΔQ under different B_z at a fixed current density $j_x = 4 \times 10^{10}$ A/m^2, showing minimized skyrmion annihilation at $B_z = 300$ mT. Insets show magnetic textures at selected fields: $B_z = 0$ mT, stripe domains extend from the boundaries; $B_z = 200$ mT, skyrmions exhibit trailing tails; $B_z = 400$ mT, skyrmions shrink and annihilate.

(G) Current-dependent stability regions of different skyrmion states: SKL, conformal SKL, and residual conformal SKL.

formation of a continuous and well-defined conformal SKL. In contrast, at $B_z = 300$ mT, Q remains nearly constant, suggesting an optimal balance that minimizes annihilation and enables robust conformal SKL development. Conformal SKL stability is also strongly dependent on current density, with a broad stability window ranging from 3.5×10^{10} to 15×10^{10} A/m^2 at 300 mT (Figures 1G and S4). Robust conformal SKL can be obtained across a wide range of Gilbert damping constant α from 0.3 to 0.05 (Figure S5).

Inverse mapping and force analysis reveal conformal order

To verify the conformal nature of the resulting skyrmion structures, we apply a machine-vision-based analysis to extract and quantify the underlying lattice geometry in Figure 1. Skyrmion positions are identified through edge-adjacency detection, followed by polygonal feature extraction to reconstruct the lattice topology (see methods for details). Figure 2A shows the spatial distribution of polygonal cells assigned to each skyrmion, where hexagons dominate regular regions, while pentagons (red) and heptagons (purple) emerge in compressed or distorted areas. Except for local deformed geometry, the skyrmion ensemble exhibits global conformal order. Periodically arranged curved skyrmion paths form arch-like structures (dark gray), referred to as conformal arcs, which capture both local curvature and long-range periodicity. At the upper intersection between adjacent arcs, a vertical column of skyrmions forms regular hexagonal cells that remain consistent along the column. This column, marked in light gray, is defined as the period boundary of the conformal lattice. On either side, the hexagons gradually rotate or deform, reflecting spatial variations in lattice geometry, consistent with the geometric characteristics of conformal order.[45,46]

Figures 2B and 2C track the dynamic formation of the conformal SKL under current injection, showing the temporal evolution of polygonal cell types, specifically pentagons, hexagons, and heptagons, as the system transitions from an initially uniform hexagonal SKL at t_0 to a conformal configuration. During the early stage of compression, up to $t_1 = 69$ ns, the lattice remains defect free and deforms smoothly, consistent with the constant-curvature regime observed in Figure 1D. Subtle distortions in the upper region are detected by fast Fourier transform (FFT) analysis, as shown in Figure 2C. At $t_2 = 85$ ns, pentagonal and heptagonal defects emerge from the top, accompanied by lattice slip and a ∼30° rotation confirmed by FFT, forming a distinct boundary between rotated and unrotated regions. These structural transformations mainly result from sudden changes in

Please cite this article in press as: Zhao et al., Dynamically resolved evolution and quantitative mapping of conformal skyrmion lattice, Newton (2026), https://doi.org/10.1016/j.newton.2026.100443

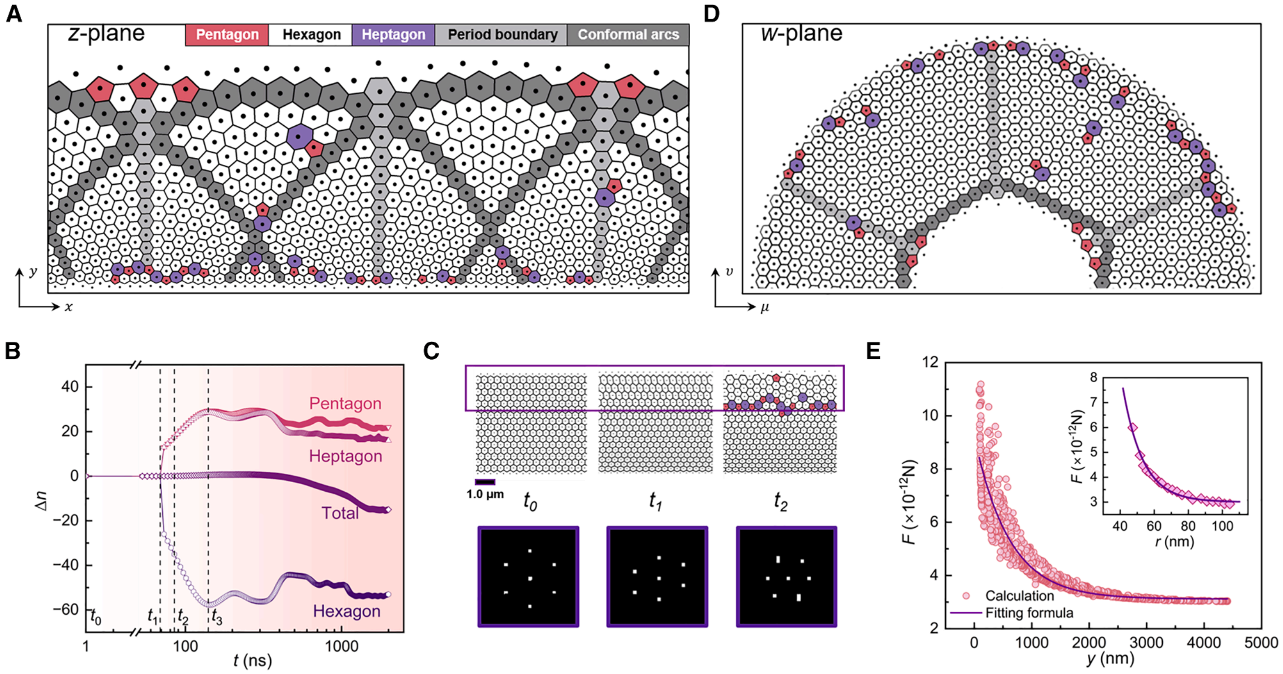

Figure 2. Inverse mapping and force analysis reveal conformal order

(A) Skyrmion distribution in the conformal SKL identified by machine-vision analysis in the original x-y plane (i.e., z plane). Each skyrmion is assigned a polygonal cell based on local coordination, with pentagons (red), hexagons (gray), and heptagons (purple) indicating varying local compressibility. Dark-gray arcs represent conformal arcs, and light-gray alignment indicates periodic boundaries.

(B) Temporal evolution of the number of pentagons, hexagons, and heptagons, as well as their total count, during current injection.

(C) Lattice evolution and corresponding FFT patterns at t_0, t_1, and t_2, a transition from an initial hexagonal lattice (t_0) to a slightly distorted structure without defects (t_1), and finally to a ∼30° rotation of the upper SKL at t_2 with a distinct defect boundary separating it from the lower region.

(D) Inverse conformal mapping applied to the conformal SKL, transforming the structure from the z plane (A) to the w plane (u-v plane), recovering a nearly perfect hexagonal lattice.

(E) Inter-skyrmion force analysis along the y direction in the conformal SKL. Inset shows the force as a function of distance r, fitted from the standard hexagonal lattice.

skyrmion spacing along the y direction, which introduce force imbalances and trigger interaction redistribution. At t_3 = 125 ns, lattice defects peak as skyrmion accumulation near the lower boundary causes strong compression, leading to defect formation and partial annihilation. The lattice then gradually reorganizes into a conformal state as order is stabilized.

We then apply an inverse conformal transformation to map the compressed configuration back to a regular hexagonal lattice (Figure 2D) to verify its conformal nature. This approach, rooted in mathematical conformal mapping, has previously been applied in particle-based systems to construct ideal conformal lattices.[9] In our compressed system, the appropriate mapping is logarithmic,[46]

$$z(w) = -(iL/\pi)\ln(i\pi w/L), \qquad \text{(Equation 1)}$$

with the inverse form

$$w(z) = -(iL/\pi)e^{i\pi z/L}, \qquad \text{(Equation 2)}$$

where $z = x + iy$ and $w = u + iv$ denote the complex planes before and after transformation, and L is the system length along the compression y direction. Applying this inverse mapping to the conformal SKL recovers a nearly perfect hexagonal lattice in the w plane, as shown in Figure 2D. In the mapped configuration (Figure 2D), residual defects are mainly distributed near the outermost ring, which corresponds to the lower compressed region in the original z plane (Figure 2A). The defects, conformal arcs (dark gray), and vertical period boundaries (light gray) exhibit a consistent spatial correspondence between the original (Figure 2A) and mapped (Figure 2D) configurations.

Furthermore, we quantify the effective skyrmion-skyrmion interaction based on energy gradients and nearest-neighbor coordination to understand the physical mechanism behind the conformal ordering (see methods for details). The extracted force-radius relationship, shown in the inset of Figure 2E, follows an exponential form: $F = A_1 e^{-r/B} + A_0$, where A_1, B, and A_0 are fitting constants. Using the y-r profile from Figure 1E and the r-a relation from Figure S6, we map the interaction onto the conformal SKL along the compression y axis, yielding the spatial force profile (Figure 2E): $F = (6.12e^{-0.0016y} + 3.12) \times 10^{-12}$ N. This expression reveals an exponentially decaying repulsive force along the y direction, which is qualitatively consistent with theoretical predictions for conformal lattice formation in particle systems.[9] The first term reflects the inter-skyrmion interaction, while the second term corresponds to a constant background force likely arising from boundary confinement.

Please cite this article in press as: Zhao et al., Dynamically resolved evolution and quantitative mapping of conformal skyrmion lattice, Newton (2026), https://doi.org/10.1016/j.newton.2026.100443

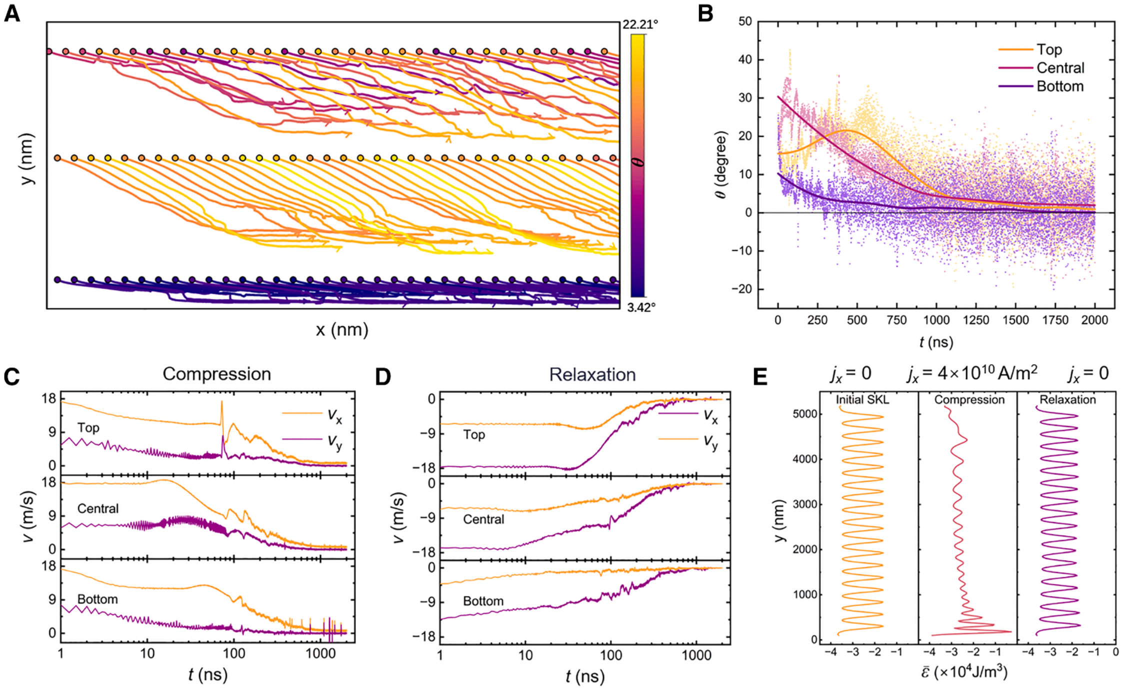

Figure 3. Trajectory, velocity, and Hall-angle responses in conformal SKL formation and relaxation

(A) Skyrmion trajectories at top, central, and bottom regions during conformal SKL formation, color coded by total Hall angles.

(B) Time evolution of the row-average skyrmion Hall angle extracted from (A), shown as scatterplots with fitted curves.

(C and D) Temporal evolution of velocity components v_x and v_y in the three regions during (C) compression and (D) relaxation.

(E) Longitudinally averaged energy density along the y axis, showing initial uniformity at $j_x = 0$, energy buildup during compression at $j_x = 4 \times 10^{10}$ A/m^2, and redistribution upon relaxation after current removal.

Layer-resolved dynamics during conformal SKL formation and relaxation

In Figure 3, we tracked the motion of all skyrmions using machine-vision algorithms and KDTree-based nearest-neighbor analysis to investigate the dynamical formation of the conformal SKL (see methods and Figure S7).[48] Figure 3A shows representative trajectories from the top, central, and bottom regions, with color encoding the total Hall angle by the end of the process. Skyrmions in the central region experience the largest transverse displacement, reaching a final Hall angle of approximately 22°, with trajectories extending over one-third of the system height. Top-layer skyrmions show moderate deflection, while bottom-layer skyrmions remain confined near the edge due to boundary repulsion. The corresponding time evolution of the instantaneous Hall angle in Figure 3B reveals distinct real-time behaviors between the top and central regions. Central skyrmions show the highest initial Hall angles of ∼30°, which gradually decline under compression. Top-layer skyrmions respond more slowly but increase steadily and eventually exceed the central layer. This reversal may arise from stronger boundary confinement in lower layers, which limits the lateral response from bottom to top.

Figures 3C and 3D further characterize the dynamical evolution during compression and relaxation, with corresponding magnetic states shown in Figure S8. At the early stage, longitudinal velocity v_x consistently dominates over the transverse component v_y across all regions, with $v_x > 2v_y$, indicating predominantly current-aligned motion. Central skyrmions sustain the highest velocities in both directions, while top and bottom skyrmions gradually slow down. By t = 1,000 ns, the entire system reaches a saturated state with $v_y \approx 0$ and $v_x \approx 0.7$ m/s, indicating strong confinement in the conformal SKL. Once the conformal lattice forms, skyrmions become effectively locked in position and are no longer easily driven by the current. After turning off the driving current, skyrmions in all layers exhibit recoil motion, with both v_x and v_y reversing sign but maintaining magnitudes similar to those of the compression phase. The ratio $|v_x| > 2|v_y|$ remains, and velocities decay layer by layer, starting from the bottom. By t = 1,000 ns post removal, all motion ceases with $v_x = v_y = 0$. This behavior is further supported by heatmaps of v_x and v_y for all skyrmions shown in Figure S7. The corresponding energy evolution is captured in Figure 3E, where energy initially accumulates near the bottom boundary for the conformal SKL due to compression and later redistributes uniformly as the system relaxes, consistent with a reversible transition into a low-energy state, as also detailed in Figures S9 and S10.

Experimental formation of conformal SKL under electric current excitation

To experimentally realize the conformal SKL, we prepare a $Co_9Zn_9Mn_2$ thin plate and investigate the current-driven skyrmion dynamics using Lorentz transmission electron microscopy (L-TEM). Skyrmions are first nucleated by applying a relatively long pulsed current (30 μs, ∼7.62 × 10^9 A/m^2) under an external magnetic field of 100 mT, where both spin-transfer torque and

Please cite this article in press as: Zhao et al., Dynamically resolved evolution and quantitative mapping of conformal skyrmion lattice, Newton (2026), https://doi.org/10.1016/j.newton.2026.100443

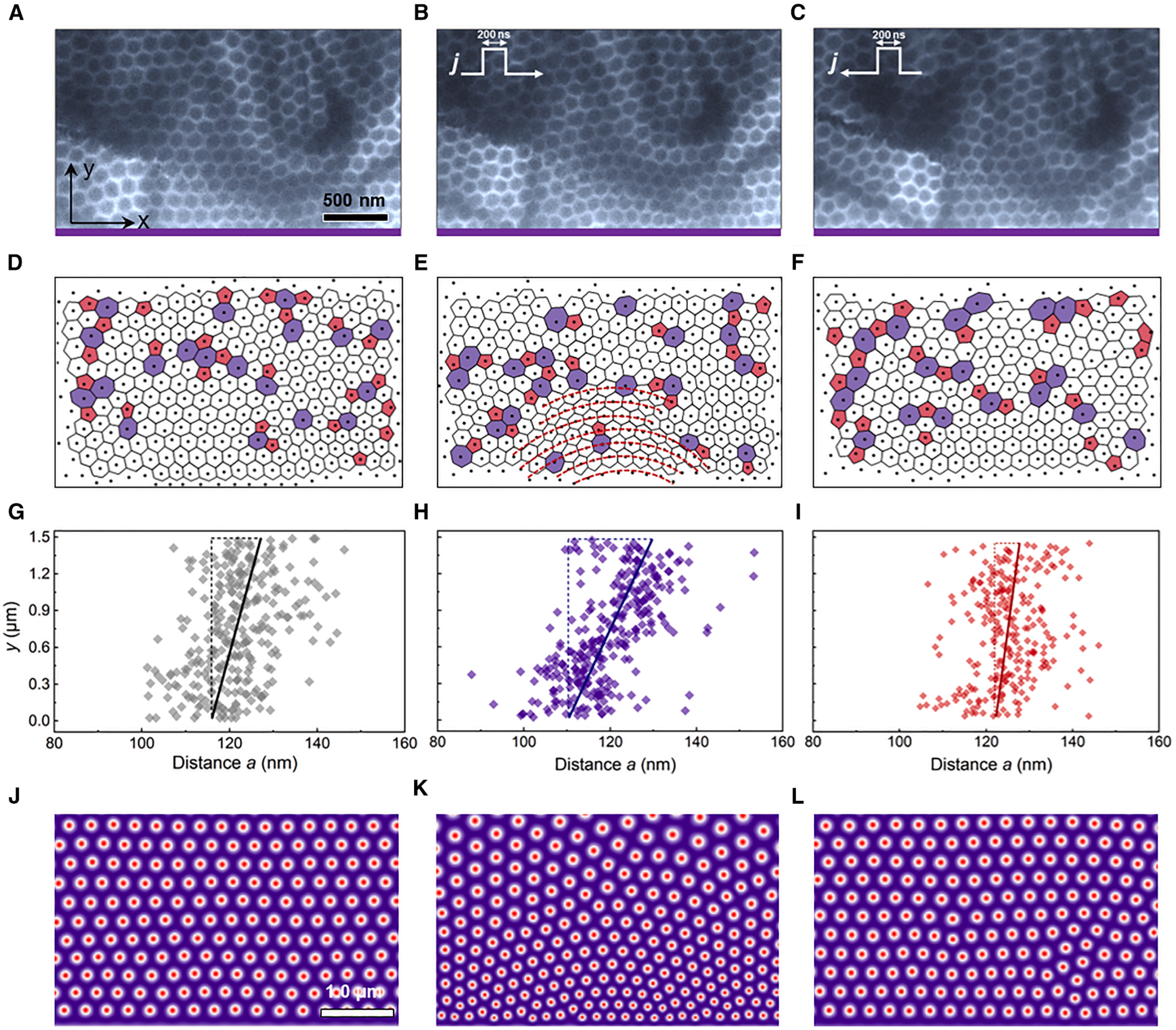

Figure 4. Experimental formation of conformal SKL under electric current excitation

(A–C) L-TEM images showing the evolution of the skyrmion lattice under pulsed current stimuli. (A) Initial skyrmion lattice generated by applying a pulsed current (~7.62 × 10^9 A/m^2, 30 μs). (B) Conformal SKL formed near the lower boundary after applying current pulses along the +*x* direction (~6.10 × 10^9 A/m^2, 500 ns, 50 repetitions). (C) Recovered hexagonal SKL after applying a reverse current (~5.75 × 10^9 A/m^2, 500 ns, 35 repetitions). The lower purple-shaded lines in the micrographs indicate the sample bottom edges.

(D–F) Machine-vision reconstructed skyrmion configurations corresponding to (A)–(C). Heptagonal and pentagonal defects are marked in purple and red, respectively. In (E), the dashed arc outlines the conformal curvature.

(G–I) Spatial distribution of skyrmion diameters along the *y* axis extracted from (D)–(F), revealing a pronounced size gradient during the formation of conformal SKL in (H).

(J–L) Micromagnetic simulations reproduce the experimental observations, including the initial SKL in (J), current-induced conformal SKL under pulses of 4 × 10^{10} A/m^2 in (K), and recovery of the hexagonal state upon current reversal in (L).

thermal heating contribute to their formation (Figure 4A). To further drive the skyrmion motion and induce deformation, nanosecond pulses (500 ns) at a current density of ~6.10 × 10^9 A/m^2 are applied for 50 repetitions (Figure 4B). The skyrmions move diagonally, not only along the current direction but also laterally toward the bottom edge, due to the skyrmion Hall effect. They accumulate at the bottom edge, causing boundary-induced compression that reduce and deform the skyrmions. Consequently, the skyrmions are reorganized into arc-shaped configurations, forming a conformal SKL. When reverse current pulses (~5.75 × 10^9 A/m^2 for 35 repetitions) are applied, the skyrmions move away from the bottom edge, and the conformal lattice gradually relaxes back into a regular hexagonal arrangement (Figure 4C).

We further apply a machine-vision pipeline to identify the experimental SKL configuration (Figures 4D–4F) and quantify

Please cite this article in press as: Zhao et al., Dynamically resolved evolution and quantitative mapping of conformal skyrmion lattice, Newton (2026), https://doi.org/10.1016/j.newton.2026.100443

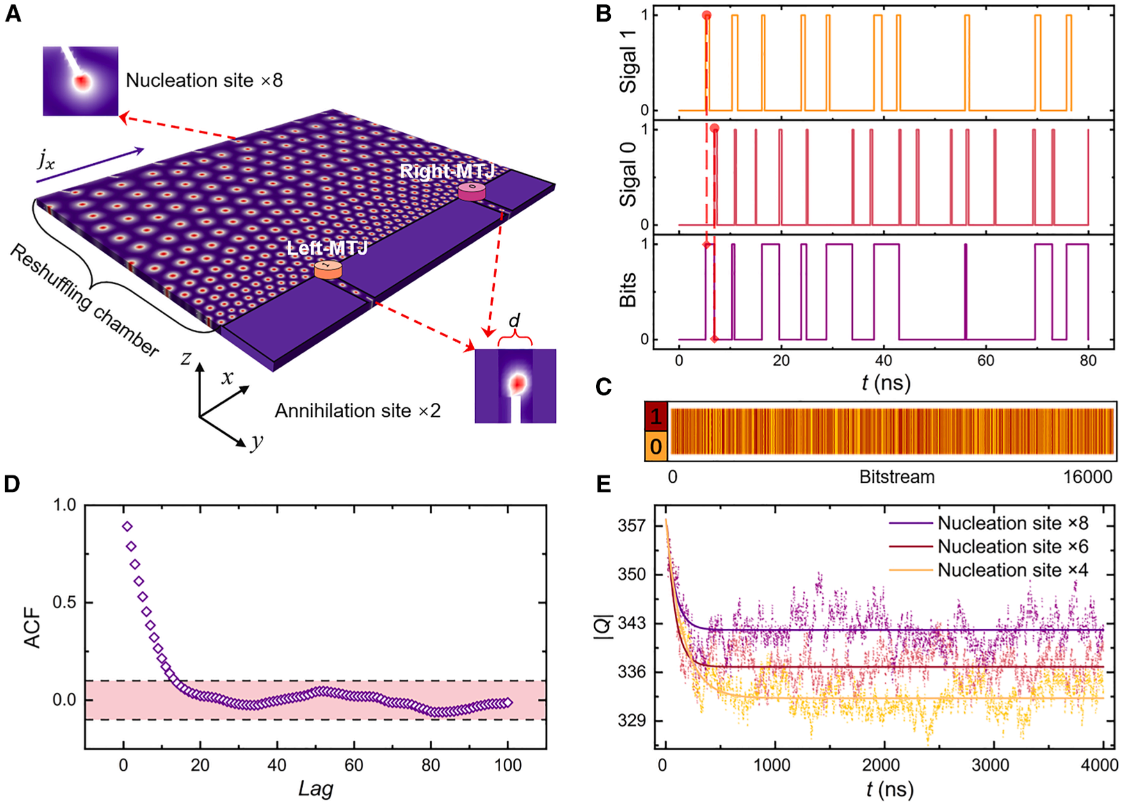

Figure 5. Conformal SKL-based true random-number generator

(A) Schematic of the true random-number generator design: skyrmions are compressed in a reshuffling chamber by a current j_x and enter one of two output channels equipped with magnetic tunnel junction (MTJ), where left and right detections are recorded as "1" and "0." Detected skyrmions are annihilated at notched exits. Eight nucleation sites at the top provide continuous skyrmion injection.

(B) Detection signals from the two MTJs for the first 80 ns. Orange and red pulses represent skyrmions detected by the left MTJ and right MTJ, corresponding to binary "1" and "0." The resulting bitstream is shown as a purple line, constructed from the event sequence. The red dashed lines indicate the corresponding transition points at which the bit-0 and bit-1 channels switch on and begin contributing to the combined bitstream.

(C) Random bitstream generated from 16,000 events. Red and orange lines represent "1" and "0," respectively.

(D) Autocorrelation of the bitstream for lag orders k, with the range of 15–100 showing all values within 0 ± 0.10, which reflects low correlation.

(E) Total topological number evolution for devices with four (orange), six (magenta), and eight (red) nucleation sites. The number decreases initially and stabilizes as injection and output balance.

the skyrmion size distribution (Figures 4G–4I). Multiple pentagon and heptagon defects are observed throughout the sample (Figures 4D–4F), which may arise from intrinsic Mn disorder in the Co-Zn-Mn system[49] and from a metastable state away from thermal equilibrium.[50] The skyrmion sizes show a relatively uniform distribution at the beginning of the pulse sequence, consistent with the small overall slope in the scatterplot in Figure 4G. With increasing pulse number, a clear size gradient develops (Figure 4H), manifested by a steeper slope and the emergence of a conformal lattice near the bottom edge (Figure 4E). Applying a reverse current relaxes the skyrmions, restores a more uniform size distribution, and consequently disrupts the conformal ordering.

Given the noticeable defects observed in the experimental sample, we perform additional numerical simulations incorporating randomly distributed pinning defects (Figures 4J–4L, see methods). Current pulses drive the lattice from an initial hexagonal state (Figure 4J) into a conformal SKL with a size gradient near the bottom edge (Figure 4K), while reversing the current relaxes it toward a hexagonal lattice (Figure 4L). The consistency between simulation and experiment confirms the physical viability of conformal SKL formation under current-induced compression.

Conformal SKL-based true random-number generator

Motivated by the conformal SKL evolution dynamics, we propose a true random-number generator (TRNG) that utilizes skyrmion interactions and dynamic reshuffling to produce bitstreams. Figure 5A presents a schematic of our designed TRNG, consisting of a square reshuffling chamber that serves as the compression zone along with two output channels symmetrically located at one-quarter and three-quarters of the chamber's width along the x axis. A direct current of $j_x = 1 \times 10^{11}$ A/m^2 is applied to drive skyrmion motion, inducing frequent collisions and many-body interactions within the chamber. These interactions, enhanced by the skyrmion Hall effect, lead to lateral compression and a spatial size gradient in the skyrmion ensemble. To emulate current-induced thermal fluctuations, thermal noise corresponding

Please cite this article in press as: Zhao et al., Dynamically resolved evolution and quantitative mapping of conformal skyrmion lattice, Newton (2026), https://doi.org/10.1016/j.newton.2026.100443

to 50 K was included in the simulations to enhance trajectory unpredictability and output entropy.

Figure 5B shows representative detection signals from the two magnetic tunnel junctions (MTJs) placed at the entrances of the output channels. Red pulses from the left MTJ correspond to binary “1,” and orange pulses from the right MTJ correspond to binary “0.” Once the compressed skyrmion diameter satisfies $2r < d$, where d is the channel width, individual skyrmions enter either output channel and are detected by the corresponding MTJ. These events generate a bitstream that flips upward or downward based on which channel is triggered, as shown in the purple square waveform in Figure 5B. A real-time visualization of skyrmions exiting the output channels can be found in Video S2. To maintain stable operation, eight elongated nucleation sites at the top of the device continuously inject skyrmions. After detection, skyrmions are directed toward notched exits where they are annihilated, completing a continuous cycle of skyrmion injection, detection, and removal. A full 16,000-bit stream is visualized in Figure 5C, with vertical red and orange lines marking “1” and “0” bits, respectively.

To evaluate statistical randomness, we compute the Shannon information entropy,[51]

$$S = -p_0 \log_2 p_0 - p_1 \log_2 p_1, \qquad \text{(Equation 3)}$$

where p_0 and p_1 are the relative probabilities of “0” and “1.” The measured bitstream yields $p_1 = 50.6\%$, corresponding to a Shannon entropy of 0.99989, close to the theoretical maximum of 1 for a perfectly random source. Entropy values computed over 8,000 and 4,000 bits are 0.9996 and 0.9937, respectively, showing that the entropy increases with bitstream length and steadily converges toward 1. To access temporal randomness, we calculate the normalized autocorrelation function (ACF):

$$\mathrm{ACF}(k) = \frac{\sum_{t=1}^{N-k} (x_t - \bar{x})(x_{t+k} - \bar{x})}{\sum_{t=1}^{N} (x_t - \bar{x})^2}, \qquad \text{(Equation 4)}$$

where $x_t \in \{1,0\}$ is the bit value at time t, $\bar{x}$ is the mean of the bitstream, N is the total number of bits, and k is the lag order of bitstream. Ideally, $\mathrm{ACF}(k) \approx 0$ for $k > 0$, indicating no temporal correlation and thus strong randomness. As shown in Figure 5D, the autocorrelation function exhibits noticeable values at short lags ($k < 15$), reflecting short-range correlations inherent to the bit-generation process. Beyond this regime, all values rapidly decay and remain within 0 ± 0.10 for $k = 15$–100, confirming the absence of long-range correlations and the overall statistical quality of the output. Furthermore, the bit sequences are evaluated using the National Institute of Standards and Technology randomness test,[52,53] both in the presence and absence of defects. Our TRNG successfully passed the tests, meeting the required statistical criteria (supplemental information).

Meanwhile, we monitored the evolution of the system’s total topological number during operation. As shown in Figure 5E, the number initially drops sharply due to skyrmion annihilation at the boundary. It then stabilizes as the system reaches a steady conformal lattice and the rates of skyrmion nucleation and output approach dynamic equilibrium, enabling continuous and stable bitstream generation. Sustaining such a steady state via notch-assisted nucleation/annihilation may increase additional energy dissipation and local Joule heating, potentially affecting device reliability. The process typically requires current densities of $\sim 10^{10}$–10^{12} A/m^2 depending on the notch geometry and current pulse width.[25,28,54] We further investigate the impact of nucleation site count (4, 6, and 8), finding that reducing the number lowers the final steady-state topological number, effectively acting as different TRNG “seeds.” The same conformal framework can be extended to enable additional functionalities, including skyrmion-based memory and dynamic sensing applications, as illustrated in Figure S11.

DISCUSSION

We have investigated the compression-induced formation of a conformal SKL through direct tracking of its dynamic evolution in micromagnetic simulations and have further verified its formation and reversible control experimentally. Real-time trajectory analysis employing machine vision uncovers layer-dependent Hall-angle redistribution and sequential velocity decay, collectively mediating the reorganization of skyrmions. Detailed analysis demonstrates the evolution of lattice curvature, generation of topological defects, and the presence of an exponentially decaying repulsive force along the compression axis, aligning with the boundary-mediated gradient essential for stabilizing the conformal lattice arrangement. The observed compression-relaxation dynamics and collective recoil behavior underscore a reversible interaction-mediated transition into a geometrically confined conformal state. Additionally, the conformal nature of the lattice is mathematically confirmed through the application of logarithmic transformations.

Importantly, we experimentally observe the conformal SKL in chiral-lattice magnet $Co_9Zn_9Mn_2$, which has previously been explored mainly in theoretical studies of particle systems,[9,46] superconducting vortices,[47] and skyrmion ensembles.[10] Under nanosecond current pulses, the conformal SKL can be reversibly manipulated and shows qualitative agreement with our simulations. The observed conformal ordering represents a current-driven, locally ordered phase that is distinct from the solid-to-liquid transitions of skyrmion lattices induced by temperature or magnetic fields.[3,8] Our combined experimental and simulation results thus establish skyrmion Hall motion and boundary compression as effective means to control collective skyrmion dynamics and ordering. The accompanying gradients in skyrmion size and density further provide a geometry-tunable source of stochasticity for true random-number generation (Figure 5). In real materials, disorder and defects (Figure 4) may partially reduce conformal ordering and influence collective motion. Future research along the direction could examine topological-defect dynamics during conformal SKL formation and explore low-pinning material platforms toward practical spintronic implementations.

METHODS

Micromagnetic simulations for conformal skyrmion lattice

We carried out micromagnetic simulations using the Mumax3 package, which numerically solves the Landau-Lifshitz-Gilbert equation with Zhang-Li spin-transfer torque (STT) in the current in-plane injection[55]:

$$\frac{d\mathbf{m}}{dt} = -\gamma\mathbf{m}\times\mathbf{H}_{\text{eff}} + \alpha\mathbf{m}\times\frac{d\mathbf{m}}{dt} + \boldsymbol{\tau}_{\text{STT}}. \qquad \text{(Equation 5)}$$

Here, $\mathbf{m}$ is the normalized magnetization, γ is the gyromagnetic ratio, α is the Gilbert damping parameter, and $\mathbf{H}_{\text{eff}}$ is the effective magnetic field derived from the system's energy contributions. The STT term is defined as $\tau_{\text{STT}} = -(\mathbf{v}_s\cdot\nabla)\mathbf{m} + \beta\mathbf{m}\times(\mathbf{v}_s\cdot\nabla)\mathbf{m}$, where $\mathbf{v}_s = -\mu_B p/[eM_s(1+\beta^2)]\mathbf{j}$, with μ_B the Bohr magneton, p the spin polarization, e the electron charge, M_s the saturation magnetization, $\mathbf{j}$ the current density, and β the nonadiabatic spin torque parameter.

The simulation parameters were chosen to approximate the effective magnetic properties of the Co-Zn-Mn chiral magnet system, as reported in previous experiments[55,56]: saturation magnetization $M_s = 1.1\times10^5$ A/m, exchange stiffness $A_{ex} = 2.8\times10^{-11}$ J/m, bulk DMI constant $D = 1.2\times10^{-3}$ J/m^2, and the non-adiabaticity $\beta = 0.01$. The simulation grid size in Figure 1 was set to 512 × 256 × 8, with a uniform cubic cell size of 20 nm, which is smaller than the magnetic exchange length $\sqrt{2A_{ex}/\mu_0 M_s{}^2}\sim 60$ nm, and periodic boundary conditions were applied along the x direction only. To simulate the conformal SKL pattern with three period lengths (Figure 2A), the x-direction grid size increased to 614 to accommodate the spatial distribution. To facilitate the formation of well-defined conformal SKL, a relatively high damping coefficient ($\alpha = 0.3$) was used in Figures 1, 2, 3, and 5. In contrast, Figure 4 employed a more experimentally realistic value ($\alpha = 0.1$)[57] and incorporated randomly distributed cubic pinning defects (20 nm per side), modeled via locally enhanced uniaxial anisotropy K_u. The defect concentration was 0.953%, with strengths randomly sampled from 0 to 1×10^5 J/m^3. For the simulation in Figure 4K, a pulsed current was applied along the x direction ($|j| = 4\times10^{10}$ A/m^2, 15 pulses, 50 ns on/5 ns off). In Figure 4L, the current was reversed ($|j| = 4\times10^{10}$ A/m^2, 5 pulses, 10 ns on/10 ns off). For the TRNG structure (Figure 5), the grid size was set to 400 × 300 × 8. Narrow nucleation notches in TRNG device were introduced at 60° to the edge to facilitate efficient skyrmion generation. The detection channel dimensions were set to 100 nm in width and 1,000 nm in length, with two MTJ detections positioned at the channel exit. To impose rigid boundary conditions, a perpendicular uniaxial anisotropy of $K_u = 7\times10^4$ J/m^3 was applied on both sides of the channel. The simulations used the built-in *relax*() function in Mumax3 with the adaptive RK45 solver,[55] which automatically adjusts the time step via error control. During the relaxation, the time step remained within 9×10^{-13} s and 1.2×10^{-12} s, which is safely below the typical precession timescale (tens of picoseconds).

Graph-based analysis of curvature and lattice geometry

To extract the curvature of the conformal SKL in Figure 1, we employed a graph-based image processing pipeline (see Figure S1). Parameter optimization for this method was performed in Figure S2. First, the out-of-plane magnetization m_z was averaged over the thickness and converted into an 8-bit gray map. Skyrmion cores were identified using Otsu's thresholding (threshold value: 160) and filtered by connected-component labeling. A Delaunay triangulation was performed on the skyrmion centroids, removing excessively long edges and triangles with angles larger than 100° to reduce boundary effects. The triangulation was then converted into a graph using NetworkX, where nodes represent skyrmions connected to their neighbors. Smooth conformal SKL paths were formed by merging approximately collinear edges (angular tolerance ±25°) using a Union-Find algorithm. Nodes with three connections were pruned, and only edge chains with at least 20 segments were retained. Each chain was ordered by depth-first traversal, yielding point sequence $\{\mathbf{r}_i\}$. The local curvature ρ_i was calculated using a ten-point sliding window as

$$\rho_i = \frac{2|(\mathbf{r}_i-\mathbf{r}_{i-5})\times(\mathbf{r}_{i+4}-\mathbf{r}_i)|}{|\mathbf{r}_i-\mathbf{r}_{i-5}|\cdot|\mathbf{r}_{i+4}-\mathbf{r}_i|\cdot|\mathbf{r}_{i+4}-\mathbf{r}_{i-5}|}. \qquad \text{(Equation 6)}$$

To extract the lattice geometry of conformal SKL in Figure 2A, triangle centroids from the Delaunay triangulation were used as lattice nodes, and edge adjacency was determined based on shared triangle edges. A binary image of centroid connections was then used to detect closed polygonal cells via contour detection and polygonal approximation (cv2.approxPolyDP). Polygons were retained only if they met specific geometric criteria: (1) all interior angles ≥80°, (2) difference between the maximum and minimum angles smaller than the average angle, and (3) exclusion of cells near image boundaries or with high angular distortion. The validated polygons, classified by their number of sides, were color coded to visualize local lattice distortions and quantify topological defects.

ESTIMATION OF INTER-SKYRMION FORCES IN THE CONFORMAL SKL

To estimate the interaction force between skyrmions within the lattice shown in Figure 2A, we analyzed how energy varies with skyrmion size under compression. Starting from a stable hexagonal lattice, we slightly increased the magnetic field $B + \delta B$, resulting in a small change in the skyrmion radius from r to $r + \delta r$. The field was then reset to the original B and the system relaxed to a new equilibrium, with energy decreasing from $E + \delta E$ to E. Assuming the effective interaction distance is determined by the lattice spacing a, the interaction force can be approximated using the energy gradient

$$F = -|\nabla E|\frac{1}{6N}\approx-\frac{\delta E}{\delta a}\frac{1}{6N} = -\frac{\delta E}{\delta r}\frac{\delta r}{\delta a}\frac{1}{6N}, \qquad \text{(Equation 7)}$$

where N is the number of skyrmions, and the factor 1/6 accounts for six nearest-neighbor interactions. The relation between radius and spacing is given by $r = k + A\ln a$ with constants k and A (Figure S6), which provides the needed link between δa and δr. Finally, using the y-r relation from Figure 1E, the resulting force profile $F(y)$ in Figure 2E directly reflects the spatial variation along the y direction within the conformal SKL. This method allows efficient estimation of interaction forces for different skyrmion sizes.

Trajectory-based analysis of skyrmion velocity and Hall angle

To analyze the velocity evolution and deflection behavior of selected skyrmion rows, we first extract skyrmion positions from the initial frame within the extended non-periodic boundary, retaining only those with centers inside the original image domain. Row indices are assigned based on image height and total row count, and specific rows (e.g., rows 2, 8, and 17, corresponding to the top, central, and bottom rows as defined in Figure 3) are selected for analysis. Skyrmion centers are then extracted from each frame in sequence. Using a KDTree-based nearest-neighbor algorithm, skyrmions are matched frame by frame to reconstruct individual trajectories. Instantaneous velocity vectors are computed via finite differences, and the deflected Hall angle is defined as the angle between the velocity vector and the positive x axis. The mean deflected Hall angle for each row in Figure 3B is obtained by averaging over all skyrmions in that row and tracked over time to reveal directional dynamics.

Sample preparation and L-TEM observation

Bulk single crystals of $Co_9Zn_9Mn_2$ were grown using the Bridgman method.[58] A (001)-oriented thin plate was prepared via focused ion beam milling. The crystal orientation and phase purity of the fabricated thin plate were confirmed by selected-area electron diffraction and energy-dispersive X-ray spectroscopy. Real-space imaging of the skyrmion lattice was then performed using L-TEM (JEOL-F200, Japan). Pulsed voltages were introduced using an arbitrary waveform generator to drive skyrmion dynamics.

RESOURCE AVAILABILITY

Lead contact

Requests for further information and resources should be directed to and will be fulfilled by the lead contact, Licong Peng (licong.peng@pku.edu.cn).

Materials availability

This study did not generate new materials.

Data and code availability

The data and code that support the findings of this study are available from the lead contact upon reasonable request.

ACKNOWLEDGMENTS

This work is supported by the National Key Research and Development Program of China (nos. 2025YFA1411002, 2022YFA1203902, and 2022YFA1204003), Advanced Materials - National Science and Technology Major Project (no. 2025ZD0618001), the National Natural Science Foundation of China (nos. 52471249, 92263203, 12241401, 52402331, 12474122, and 52171188), Beijing Natural Science Foundation (no. F252072), and the China-Germany Collaboration Project (no. M-0199). X.Z. acknowledges support by CREST, the Japan Science and Technology Agency (grant no. JPMJCR20T1), and grants-in-aid for scientific research from JSPS KAKENHI (grant nos. JP25K17939 and JP20F20363). We thank the Materials Processing and Analysis Center at Peking University and the high-pressure synergetic measurement station (A9) of the Synergetic Extreme Condition User Facility (SECUF, https://cstr.cn/31123.02.SECUF) and the Laboratory of Microfabrication, IOP CAS, for supporting the sample microfabrication.

AUTHOR CONTRIBUTIONS

L.P., Y.H., J.Y., and G.Z. jointly supervised the work and designed the experiments; W.Z., S.L., Q.L., X.Z., G.Z., and L.P. performed the simulations and data analysis; W.Z. and S.L. carried out the theoretical analysis; S.F. and T.X. grew the single-crystal materials; Q.L., H.L., and G.H. fabricated the samples; Q.L. and W.Z. performed the L-TEM measurements; and W.Z., S.L., and L.P. drafted the manuscript with revisions from X.Z., Z.L., G.Z., J.Y., and Y.H. All authors discussed the results and contributed to the final version of the manuscript.

DECLARATION OF INTERESTS

The authors declare no competing interests.

SUPPLEMENTAL INFORMATION

Supplemental information can be found online at https://doi.org/10.1016/j.newton.2026.100443.

Received: October 10, 2025
Revised: December 26, 2025
Accepted: February 10, 2026

REFERENCES

1. Mermin, N.D. (1968). Crystalline order in two dimensions. Phys. Rev. *176*, 250–254.
2. Guillamón, I., Córdoba, R., Sesé, J., De Teresa, J.M., Ibarra, M.R., Vieira, S., and Suderow, H. (2014). Enhancement of long-range correlations in a 2d vortex lattice by an incommensurate 1d disorder potential. Nat. Phys. *10*, 851–856.
3. Huang, P., Schönenberger, T., Cantoni, M., Heinen, L., Magrez, A., Rosch, A., Carbone, F., and Rønnow, H.M. (2020). Melting of a skyrmion lattice to a skyrmion liquid via a hexatic phase. Nat. Nanotechnol. *15*, 761–767.
4. Yao, Z., and Olvera de la Cruz, M. (2013). Topological defects in flat geometry: the role of density inhomogeneity. Phys. Rev. Lett. *111*, 115503.
5. Bernard, E.P., and Krauth, W. (2011). Two-step melting in two dimensions: first-order liquid-hexatic transition. Phys. Rev. Lett. *107*, 155704.
6. J, M.K., and D, J.T. (1973). Ordering, metastability and phase transitions in two-dimensional systems. J. Phys. C Solid State Phys. *6*, 1181.
7. Meisenheimer, P., Zhang, H., Raftrey, D., Chen, X., Shao, Y.T., Chan, Y.T., Yalisove, R., Chen, R., Yao, J., Scott, M.C., et al. (2023). Ordering of room-temperature magnetic skyrmions in a polar van der waals magnet. Nat. Commun. *14*, 3744.
8. Gruber, R., Rothörl, J., Fröhlich, S.M., Brems, M.A., Kammerbauer, F., Syskaki, M.A., Jefremovas, E.M., Krishnia, S., Sudbø, A., Virnau, P., and Kläui, M. (2025). Real-time observation of topological defect dynamics mediating two-dimensional skyrmion lattice melting. Nat. Nanotechnol. *20*, 1405–1411.
9. Rothen, F., and Pierański, P. (1996). Mechanical equilibrium of conformal crystals. Phys. Rev. E *53*, 2828–2842.
10. Bellizotti Souza, J.C., Vizarim, N.P., Reichhardt, C.J.O., Reichhardt, C., and Venegas, P.A. (2023). Spontaneous skyrmion conformal lattice and transverse motion during dc and ac compression. New J. Phys. *25*, 053020.
11. Nagaosa, N., and Tokura, Y. (2013). Topological properties and dynamics of magnetic skyrmions. Nat. Nanotechnol. *8*, 899–911.
12. Fert, A., Reyren, N., and Cros, V. (2017). Magnetic skyrmions: advances in physics and potential applications. Nat. Rev. Mater. *2*, 17031.
13. Büttner, F., Moutafis, C., Schneider, M., Krüger, B., Günther, C.M., Geilhufe, J., Schmising, C.V.K., Mohanty, J., Pfau, B., Schaffert, S., et al. (2015). Dynamics and inertia of skyrmionic spin structures. Nat. Phys. *11*, 225–228.
14. Yu, X.Z., Kanazawa, N., Zhang, W.Z., Nagai, T., Hara, T., Kimoto, K., Matsui, Y., Onose, Y., and Tokura, Y. (2012). Skyrmion flow near room temperature in an ultralow current density. Nat. Commun. *3*, 988.
15. Pham, V.T., Sisodia, N., Di Manici, I., Urrestarazu-Larrañaga, J., Bairagi, K., Pelloux-Prayer, J., Guedas, R., Buda-Prejbeanu, L.D., Auffret, S., Locatelli, A., et al. (2024). Fast current-induced skyrmion motion in synthetic antiferromagnets. Science *384*, 307–312.

16. Tokura, Y., and Kanazawa, N. (2021). Magnetic skyrmion materials. Chem. Rev. *121*, 2857–2897.

17. He, B., Tomasello, R., Luo, X., Zhang, R., Nie, Z., Carpentieri, M., Han, X., Finocchio, G., and Yu, G. (2023). All-electrical 9-bit skyrmion-based racetrack memory designed with laser irradiation. Nano Lett. *23*, 9482–9490.

18. Ma, Y., Wu, D., Yan, F., Fang, X., Qin, P., Wang, L., Liu, L., Shen, L., Liu, Z., Yang, W., et al. (2025). Ultrafast and reliable domain-wall and skyrmion logic in a chirally coupled ferrimagnet. Newton *1*, 100208. https://doi.org/10.1016/j.newton.2025.100208.

19. Zhang, X., Xia, J., Zhou, Y., Zhao, G., Liu, X., Xu, Y., and Mochizuki, M. (2025). Nanofluidic logic based on chiral skyrmion flows. Proc. Natl. Acad. Sci. USA *122*, e2506204122.

20. Song, K.M., Jeong, J.S., Pan, B., Zhang, X., Xia, J., Cha, S., Park, T.E., Kim, K., Finizio, S., Raabe, J., et al. (2020). Skyrmion-based artificial synapses for neuromorphic computing. Nat. Electron. *3*, 148–155.

21. Da Câmara Santa Clara Gomes, T., Sassi, Y., Sanz-Hernández, D., Krishnia, S., Collin, S., Martin, M.B., Seneor, P., Cros, V., Grollier, J., and Reyren, N. (2025). Neuromorphic weighted sums with magnetic skyrmions. Nat. Electron. *8*, 204–214.

22. Wang, K., Zhang, Y., Bheemarasetty, V., Zhou, S., Ying, S.C., and Xiao, G. (2022). Single skyrmion true random number generator using local dynamics and interaction between skyrmions. Nat. Commun. *13*, 722.

23. Zázvorka, J., Jakobs, F., Heinze, D., Keil, N., Kromin, S., Jaiswal, S., Litzius, K., Jakob, G., Virnau, P., Pinna, D., et al. (2019). Thermal skyrmion diffusion used in a reshuffler device. Nat. Nanotechnol. *14*, 658–661.

24. Peng, L., Karube, K., Taguchi, Y., Nagaosa, N., Tokura, Y., and Yu, X. (2021). Dynamic transition of current-driven single-skyrmion motion in a room-temperature chiral-lattice magnet. Nat. Commun. *12*, 6797.

25. Yu, X.Z., Morikawa, D., Nakajima, K., Shibata, K., Kanazawa, N., Arima, T., Nagaosa, N., and Tokura, Y. (2020). Motion tracking of 80-nm-size skyrmions upon directional current injections. Sci. Adv. *6*, eaaz9744.

26. Song, D., Wang, W., Zhang, S., Liu, Y., Wang, N., Zheng, F., Tian, M., Dunin-Borkowski, R.E., Zang, J., and Du, H. (2024). Steady motion of 80-nm-size skyrmions in a 100-nm-wide track. Nat. Commun. *15*, 5614.

27. He, Z., Li, Z., Chen, Z., Wang, Z., Shen, J., Wang, S., Song, C., Zhao, T., Cai, J., Lin, S.Z., et al. (2024). Experimental observation of current-driven antiskyrmion sliding in stripe domains. Nat. Mater. *23*, 1048–1054.

28. Iwasaki, J., Mochizuki, M., and Nagaosa, N. (2013). Current-induced skyrmion dynamics in constricted geometries. Nat. Nanotechnol. *8*, 742–747.

29. Juge, R., Sisodia, N., Larrañaga, J.U., Zhang, Q., Pham, V.T., Rana, K.G., Sarpi, B., Mille, N., Stanescu, S., Belkhou, R., et al. (2022). Skyrmions in synthetic antiferromagnets and their nucleation via electric current and ultra-fast laser illumination. Nat. Commun. *13*, 4807.

30. Yasin, F.S., Masell, J., Karube, K., Kikkawa, A., Taguchi, Y., Tokura, Y., and Yu, X. (2022). Real-space determination of the isolated magnetic skyrmion deformation under electric current flow. Proc. Natl. Acad. Sci. USA *119*, e2200958119.

31. Litzius, K., Leliaert, J., Bassirian, P., Rodrigues, D., Kromin, S., Lemesh, I., Zazvorka, J., Lee, K.J., Mulkers, J., Kerber, N., et al. (2020). The role of temperature and drive current in skyrmion dynamics. Nat. Electron. *3*, 30–36.

32. Zhou, Y., Li, S., Liang, X., and Zhou, Y. (2025). Topological spin textures: basic physics and devices. Adv. Mater. *37*, 2312935.

33. Du, H., Zhao, X., Rybakov, F.N., Borisov, A.B., Wang, S., Tang, J., Jin, C., Wang, C., Wei, W., Kiselev, N.S., et al. (2018). Interaction of individual skyrmions in a nanostructured cubic chiral magnet. Phys. Rev. Lett. *120*, 197203.

34. Deák, A., Simon, E., Yanes, R., Udvardi, L., Szunyogh, L., Nowak, U., and Rózsa, L. (2016). Skyrmions with attractive interactions in an ultrathin magnetic film. Phys. Rev. Lett. *117*, 157205.

35. Takeda, H., Kawano, M., Tamura, K., Akazawa, M., Yan, J., Waki, T., Nakamura, H., Sato, K., Narumi, Y., Hagiwara, M., et al. (2024). Magnon thermal hall effect via emergent SU(3) flux on the antiferromagnetic skyrmion lattice. Nat. Commun. *15*, 566.

36. Jin, Z., Yao, X., Wang, Z., Yuan, H.Y., Zeng, Z., Wang, W., Cao, Y., and Yan, P. (2023). Nonlinear topological magnon spin hall effect. Phys. Rev. Lett. *131*, 166704.

37. Kurumaji, T., Nakajima, T., Hirschberger, M., Kikkawa, A., Yamasaki, Y., Sagayama, H., Nakao, H., Taguchi, Y., Arima, T.H., and Tokura, Y. (2019). Skyrmion lattice with a giant topological hall effect in a frustrated triangular-lattice magnet. Science *365*, 914–918.

38. Jiang, W., Zhang, X., Yu, G., Zhang, W., Wang, X., Benjamin Jungfleisch, M., Pearson, J.E., Cheng, X., Heinonen, O., Wang, K.L., et al. (2017). Direct observation of the skyrmion hall effect. Nat. Phys. *13*, 162–169.

39. Peng, L., Yasin, F.S., Karube, K., Kanazawa, N., Taguchi, Y., Tokura, Y., and Yu, X. (2025). In-situ l-TEM observations of dynamics of nanometric skyrmions and antiskyrmions. Nano Today *62*, 102698.

40. Zhang, X., Zhao, G.P., Fangohr, H., Liu, J.P., Xia, W.X., Xia, J., and Morvan, F.J. (2015). Skyrmion-skyrmion and skyrmion-edge repulsions in skyrmion-based racetrack memory. Sci. Rep. *5*, 7643.

41. Raab, K., Brems, M.A., Beneke, G., Dohi, T., Rothörl, J., Kammerbauer, F., Mentink, J.H., and Kläui, M. (2022). Brownian reservoir computing realized using geometrically confined skyrmion dynamics. Nat. Commun. *13*, 6982.

42. Iwasaki, J., Koshibae, W., and Nagaosa, N. (2014). Colossal spin transfer torque effect on skyrmion along the edge. Nano Lett. *14*, 4432–4437.

43. Zhang, X., Xia, J., and Liu, X. (2022). Structural transition of skyrmion quasiparticles under compression. Phys. Rev. B *105*, 184402.

44. Reichhardt, C., Ray, D., and Reichhardt, C.J.O. (2015). Reversible ratchet effects for vortices in conformal pinning arrays. Phys. Rev. B *91*, 184502.

45. Ray, D., Olson Reichhardt, C.J., Jankó, B., and Reichhardt, C. (2013). Strongly enhanced pinning of magnetic vortices in type-II superconductors by conformal crystal arrays. Phys. Rev. Lett. *110*, 267001.

46. Menezes, R.M., and Silva, C.C.D.S. (2017). Conformal vortex crystals. Sci. Rep. *7*, 12766.

47. Lyu, Y.Y., Jiang, J., Wang, Y.L., Xiao, Z.L., Dong, S., Chen, Q.H., Milošević, M.V., Wang, H., Divan, R., Pearson, J.E., et al. (2021). Superconducting diode effect via conformal-mapped nanoholes. Nat. Commun. *12*, 2703.

48. Bentley, J.L. (1975). Multidimensional binary search trees used for associative searching. Commun. ACM *18*, 509–517.

49. Karube, K., White, J.S., Morikawa, D., Dewhurst, C.D., Cubitt, R., Kikkawa, A., Yu, X., Tokunaga, Y., Arima, T.H., Rønnow, H.M., et al. (2018). Disordered skyrmion phase stabilized by magnetic frustration in a chiral magnet. Sci. Adv. *4*, eaar7043.

50. Karube, K., White, J.S., Reynolds, N., Gavilano, J.L., Oike, H., Kikkawa, A., Kagawa, F., Tokunaga, Y., Rønnow, H.M., Tokura, Y., and Taguchi, Y. (2016). Robust metastable skyrmions and their triangular–square lattice structural transition in a high-temperature chiral magnet. Nat. Mater. *15*, 1237–1242.

51. Lombardi, O., Holik, F., and Vanni, L. (2016). What is shannon information? Synthese *193*, 1983–2012.

52. Bassham, L., Rukhin, A., Soto, J., Nechvatal, J., Smid, M., Leigh, S., Levenson, M., Vangel, M., Heckert, N., and Banks, D. (2010). A Statistical Test Suite for Random and Pseudorandom Number Generators for Cryptographic Applications (NIST). Special Publication 800-22 Rev. 1a.

53. Zhang, Z., Lin, K., Zhang, K., Feng, X., Chen, L., Zhang, Y., Bournel, A., Kläui, M., Zhao, W., and Zhang, Y. (2024). Ultra-fast true random number generator based on ill-posedness nucleation of skyrmion bags in ferrimagnets. IEEE Electron Device Lett. *45*, 917–920.

54. Wang, W., Song, D., Wei, W., Nan, P., Zhang, S., Ge, B., Tian, M., Zang, J., and Du, H. (2022). Electrical manipulation of skyrmions in a chiral magnet. Nat. Commun. *13*, 1593.

Please cite this article in press as: Zhao et al., Dynamically resolved evolution and quantitative mapping of conformal skyrmion lattice, Newton (2026), https://doi.org/10.1016/j.newton.2026.100443

55. Vansteenkiste, A., Leliaert, J., Dvornik, M., Helsen, M., Garcia-Sanchez, F., and Van Waeyenberge, B. (2014). The design and verification of MuMax3. AIP Adv. *4*, 107133.

56. Takagi, R., Morikawa, D., Karube, K., Kanazawa, N., Shibata, K., Tatara, G., Tokunaga, Y., Arima, T., Taguchi, Y., Tokura, Y., and Seki, S. (2017). Spin-wave spectroscopy of the Dzyaloshinskii-Moriya interaction in room-temperature chiral magnets hosting skyrmions. Phys. Rev. B *95*, 220406.

57. Preißinger, M., Karube, K., Ehlers, D., Szigeti, B., Krug Von Nidda, H.A., White, J.S., Ukleev, V., Rønnow, H.M., Tokunaga, Y., Kikkawa, A., et al. (2021). Vital role of magnetocrystalline anisotropy in cubic chiral skyrmion hosts. npj Quantum Mater. *6*, 65.

58. Tokunaga, Y., Yu, X.Z., White, J.S., Rønnow, H.M., Morikawa, D., Taguchi, Y., and Tokura, Y. (2015). A new class of chiral materials hosting magnetic skyrmions beyond room temperature. Nat. Commun. *6*, 7638.